Title
Stable carrier generation and phase-resolved digital data processing in optical coherence tomography.

Journal
Applied optics, 40(31)

ISSN
1559-128X

Authors
de Boer, JF
Saxer, CE
Nelson, JS

Publication Date
2001-11-01

DOI
10.1364/ao.40.005787

Stable carrier generation and phase-resolved digital data processing in optical coherence tomography

Johannes F. de Boer, Christopher E. Saxer, and J. Stuart Nelson

We present a technique for improved carrier generation by eliminating the instability of a mechanical device in favor of an electro-optical phase modulator in the reference arm of an optical coherence tomography system. A greater than threefold reduction in the phase variance between consecutive *A*-line scans at a repetition rate of 1 kHz was achieved. Stable and reproducible interference fringe generation permits phase-resolved digital data processing. A correction algorithm was applied to the interferometric signal to compensate for the departure of the source spectrum from an ideal Gaussian shape, resulting in up to 8-dB sidelobe suppression at the expense of a 1-dB increase in the noise floor. In addition, we could eliminate completely the broadening effect of group-delay dispersion on the coherence function by introducing a quadratic phase shift in the Fourier domain of the interferometric signal.

OCIS codes: 170.4500, 120.5050, 170.0170, 170.3010, 120.5060.

Optical coherence tomography (OCT) is an attractive technique for noninvasive imaging of biological tissue up to a depth of 2 mm with a spatial resolution of 3–10 μm.[1,2] The technique is based on the principle of low-temporal-coherence Michelson interferometry, whereby interference fringes are formed when the optical path length of light reflected from the sample matches that from the reference to within the coherence length of the source light. Scanning the length of the reference arm results in localized interference fringes with an amplitude that corresponds to sample reflectivity. Several methods for fast scanning have been developed, but all methods used so far have incorporated mechanical devices to scan both depth and generate the interference fringe carrier. One method uses a rapid-scanning optical delay (RSOD) line, which creates separately controllable phase and group delays. As described by Tearney *et al.*,[3] when the source spectrum is centered on the pivoting axis of the galvo-mounted mirror, the RSOD generates only a group delay, making it possible to generate the phase delay by other means. In this paper we implement an electro-optical phase modulator in the reference arm to generate a stable interference fringe carrier frequency.

The essential components for phase stability in the experimental setup are shown in Fig. 1; a more extensive description of the system is provided in Ref. 5. Describing the electric fields by $E(t, z) = \int A(\omega) \exp[i(\omega t - kz)]\mathrm{d}\omega$ with $\langle A(\omega)A^*(\omega')\rangle = S(\omega)\delta(\omega - \omega')$ where $S(\omega)$ denotes the source spectrum, we can give the interference term of the expression for the intensity at the detector as

$$I(t, \Delta z) \propto \int S(\omega)\exp\{i[2k\Delta z + \phi_D(\omega, t)]\}\mathrm{d}\omega + \text{c.c.} \tag{1}$$

The first term in the exponent, $2k\Delta z$, represents the phase that is due to the path-length difference Δz between the sample and reference arms. The second phase term, ϕ_D, combines contributions from the delay line and phase modulator (see Fig. 1) and is given by

$$\phi_D(\omega, t) = \frac{4\alpha t x\omega}{c} + \frac{8\pi\alpha t f\Delta\omega}{\omega s} + \frac{4y\omega}{c}\cos\left(\frac{2\pi c\Delta\omega}{{\omega_0}^2 s}\right) - \frac{8\pi y\,\tan(\Theta)}{s}\tan^2\left(\frac{2\pi c\Delta\omega}{{\omega_0}^2 s}\right) + \beta t, \tag{2}$$

where ω is the angular frequency of the light, $\Delta\omega = \omega - \omega_0$, α is the angular velocity of the galvo mirror,

When this research was performed, the authors were with the Beckman Laser Institute and Medical Clinic, University of California, Irvine, California 92612. J. F. de Boer (deboer@helix.mgh.harvard.edu) is currently with Wellman Laboratories of Photomedicine, 50 Blossom Street, BAR 724, Massachusetts General Hospital, Harvard Medical School, Boston, Massachusetts 02114.

Received 13 February 2001.
0003-6935/01/315787-04$15.00/0

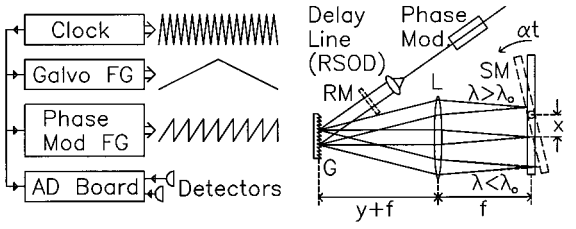

Fig. 1. Schematic of the clock synchronization of the function generators (FG) and the analog-to-digital (AD) board and the RSOD line and phase modulator. Waveforms generated by the FGs are shown (timing not to scale). In our experimental configuration, the spectrum is centered on a scanning mirror (SM), i.e., $x = 0$. Phase Mod., $LiNbO_3$ phase modulator; G, grating; L, lens; f, focal length (10 cm); y, displacement of grating from focal plane; SM, galvo-mounted scanning mirror; λ_0, center wavelength of source; αt, scan angle of mirror; x, lateral displacement of pivoting axis of SM with respect to position of the center wavelength; RM, return mirror that reflects the light back for a double pass through the delay line.

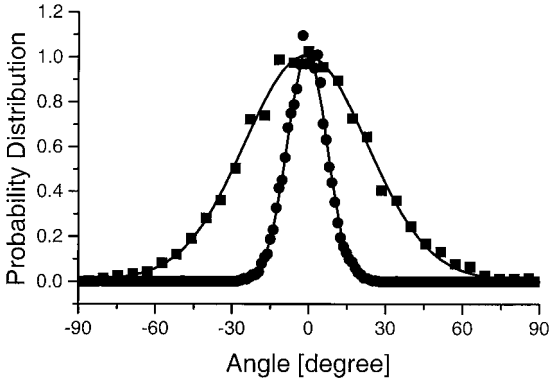

Fig. 2. Probability distribution of phase noise for mechanical and electro-optical carrier generations. The distribution of phase differences between adjacent A-line scans, determined at the reflectivity peak of a single surface, is shown. Squares, mechanical carrier generation that we obtained by displacing the pivoting axis of the scanning mirror with respect to the center wavelength ($x \neq 0$); circles, electro-optical generation of the carrier by the phase modulator only ($x = 0$); solid curves, Gaussian fits to the data. Variance of the distribution is 25.6° and 7.9°, respectively.

(135 rad/s), x is the displacement of the center wavelength with respect to the pivoting axis of the galvo mirror, f is the lens focal length (10 cm), $s = d \cos(\Theta)$ where d is the grating spacing (150 lines/mm), Θ is the diffraction angle of the center wavelength (16.4°), y is the displacement of the grating from the focal plane of the lens, and β is the phase velocity introduced by the phase modulator. Phase delay is defined as the ratio of phase and angular frequency. Group delay and group-delay dispersion (GDD) are defined as the first- and second-order derivatives of the phase with respect to angular frequency, respectively.

The first term in Eq. (2) is used to generate the carrier frequency in Refs. 3 and 4 but is set to zero in our configuration. The second term is responsible for the group-delay scanning.[3,4] The third and fourth term contribute a constant GDD in proportion to the distance y[6]; and the last term, βt, is the carrier frequency generated by the phase modulator. We calculated a GDD of 440 fs^2/mm displacement of y. The $LiNbO_3$ waveguide phase modulator introduced a GDD that was compensated for in the RSOD.

To obtain phase stability, the analog-to-digital (AD) conversion board (12 bit, 10 MHz) and the function generators (Stanford Research DG 345) that drive the RSOD galvo and phase modulator are all synchronized by an external 10-MHz clock. This ensures that, for each A-line scan, AD conversions are taken at the exact same positions in the triangular and sawtooth waveforms driving the RSOD and the phase modulator, respectively. The RSOD group-delay scanning translates the coherence function envelope, which has a width of approximately 10 μm, axially over 2.8 mm in air at a frequency of 1 kHz.

To demonstrate improved phase stability, we compared the phase variance for mechanical and electro-optical generation of the phase delay. For mechanical phase-delay generation, the spectrum of the source was displaced from the pivoting axis of the galvo mirror a distance sufficient to generate a carrier of ≈800 kHz (i.e., $x \neq 0$). For electro-optical phase-delay generation, the phase modulator was driven by a sawtooth waveform at 833 kHz, creating a 2π phase shift after double passage, and the spectrum was centered on the galvo mirror (i.e., $x = 0$). The target was a glass slide requiring the power in the sample arm to be reduced by a neutral-density filter to avoid saturation of the detectors. Phase and magnitude were obtained by digital quadrature demodulation with a spatial resolution of 5 μm. The phase difference between consecutive A-line scans at the location of the interference peak from the glass slide was calculated for three separate data sets of 1-s duration. The distributions of phase differences ($n = 3000$) for both measurements are presented in Fig. 2. The variance for mechanical and electro-optical phase-delay generation was 25.6° and 7.9°, respectively. A greater than threefold reduction in phase variance between consecutive A-line scans at a repetition rate of 1 kHz was achieved.

Digital signal processing to improve system resolution has been demonstrated previously by iterative deconvolution with the coherence envelope point response in the space domain on a two-dimensional image[7] or on a single depth profile by deconvolution with the measured power spectrum in the Fourier domain.[8] However, instabilities in the carrier frequency can alter the power spectrum and make the deconvolution unstable. Yung *et al.*[9] have shown that, even with an OCT system employing a tracking laser to monitor and correct for the reference arm mirror movement, rapid phase fluctuations that are due to, for example, vibrations could alter the spectrum considerably. The advantages of our system are high-repetition depth scanning that decreases sensitivity to low-frequency vibrations, combined with improved phase stability. We show that, by

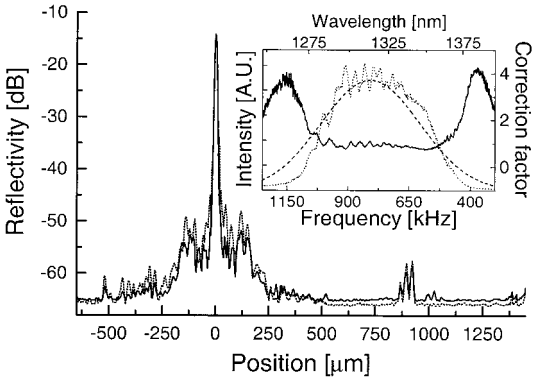

Fig. 3. Response to a single surface on a logarithmic scale as a function of distance in air. Dashed curve, uncorrected response; solid curve, response after spectral correction. Insert: power spectrum (left y axis) of the signal response to a single surface as a function of frequency (lower x axis) and the corresponding wavelength (upper x axis). Dotted curve, signal spectrum; dashed curve, fit of a Gaussian to the signal spectrum; solid curve, correction factor defined as the ratio of the Gaussian and signal spectrum (with respect to right y axis).

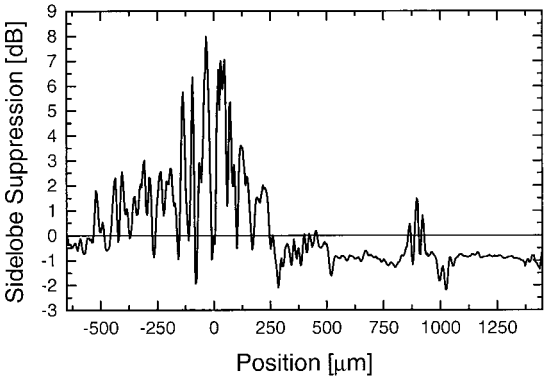

Fig. 4. Ratio of uncorrected over corrected response on a logarithmic scale, showing sidelobe suppression that can be obtained by correction of the spectral modulation shown in the insert of Fig. 3. Up to 8-dB sidelobe suppression is achieved in exchange for a 1-dB increase in the noise floor.

digital modification of the source spectrum, sidelobes that are due to spectral modulation can be suppressed.

The insert of Fig. 3 shows the source spectrum (AFC Technologies, BBS 1310, $\lambda_0 = 1310$ nm, $\Delta\lambda = 75$ nm, polarized power equals 8 mW) calculated from the power spectrum of the interferometric response to a single surface by a fast Fourier transform of each A line (4096 points). The spectrum shows modulation, which is responsible for sidelobes in the coherence envelope. We can suppress the sidelobes by modifying the source spectrum digitally. The zeroth, first, and second moment of the spectrum completely define a Gaussian function. The ratio of this ideal Gaussian and the source spectrum defines a correction curve, shown also in the insert. We obtained the spectrally filtered response of each depth profile by Fourier transforming each individual depth profile, multiplying the resulting spectrum with the correction curve, and performing the inverse transform. In Fig. 3 raw and spectrally filtered response functions to a single surface averaged over 1000 depth profiles are shown. Figure 4 shows the ratio of the filtered and unfiltered responses, smoothed over 10 μm. A sidelobe reduction of up to 8 dB can be observed, at the expense of a 1-dB increase in the noise floor far away from the main peak.

So far, to our knowledge, phase-sensitive digital signal processing for structural image enhancement has been taken advantage of only for speckle reduction.[9] Phase-sensitive digital signal processing can also be used to remove dispersion broadening of the response function in postprocessing. GDD introduces a linear dependence of the phase derivative on frequency. Third- and fourth-order dispersion would manifest itself as quadratic and cubic dependencies, respectively. Ultimately, depth-dependent sample dispersion could be corrected for. We can demonstrate GDD compensation by experimentally changing the distance y in the RSOD by -10 mm, which introduces 4.4×10^3 fs^2 GDD in the reference arm. GDD was measured by Fourier transformation of the interferometric response to a single surface. The phase of each Fourier component is calculated when we take the arc tangent of the ratio of the imaginary and real part. This method was used previously to measure and tune dispersion imbalance with dispersive elements in the interferometer arms.[2] In Fig. 5 the power spectrum and first derivative of the phase, averaged over 1000 depth profiles, are shown as a function of frequency. A linear fit to the first derivative of the phase yields a slope of 1.36×10^{-7} mrad s^2, corresponding to a 4700-fs^2 GDD. Correction for this quadratic phase shift in the Fourier domain of the interferometric

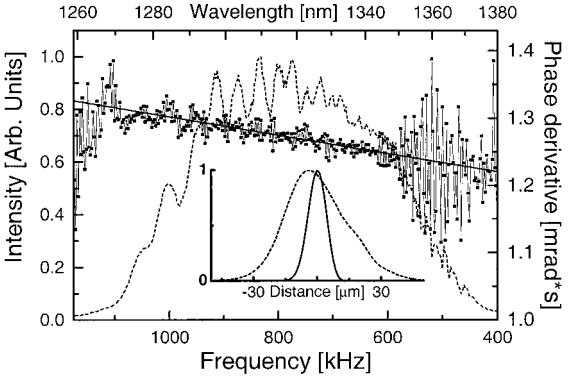

Fig. 5. Spectrum (left y axis) and phase derivative (right y axis) of the response to a single surface as a function of frequency (lower x axis) and the corresponding wavelength (upper x axis). Dashed curve, power spectrum; connected squares, derivative of the phase of the Fourier components; solid curve, linear fit to the phase derivative with slope 1.36×10^{-7} mrad s^2, which corresponds to a GDD $d^2\phi/d\omega^2 = 4700$ fs^2. Insert shows the corresponding response (coherence envelope) on a linear scale before (dashed curve, FWHM of 31.6 μm) and after (solid curve, FWHM of 10.4 μm) digital processing to remove GDD.

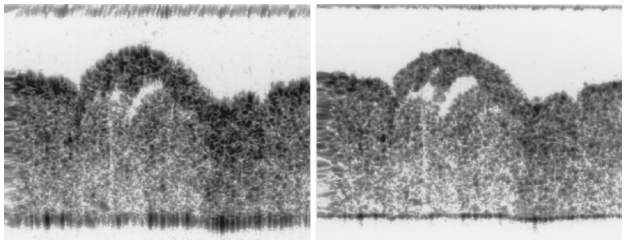

Fig. 6. Images of *ex vivo* human skin graft before and after signal processing to remove 4.4×10^3 fs^2 GDD. Left: Image blurred by GDD introduced by unbalanced dispersion in the sample and reference arm. Right: The same image after processing to eliminate GDD. GDD correction was calculated by a measurement of the dispersion imbalance before image acquisition.

signal removed the GDD in each individual depth profile. The inset of Fig. 5 shows the coherence envelope of the response to a single surface before and after digital processing, averaged over 1000 depth profiles. The resulting coherence envelope overlaps the coherence envelope of a dispersion-balanced system perfectly.

To demonstrate that GDD correction can be extended beyond the example of a single surface, we imaged a human skin graft with an unbalanced GDD system. Before imaging the skin graft, we recorded the response function of a single surface to obtain the quadratic phase correction term. The GDD unbalance in each depth profile of the image was then corrected, and the result is shown in Fig. 6. The left image shows the effect of unbalanced GDD; the right image shows the result of digital GDD compensation on the same data set. No differences were noticeable between a control image (not shown) recorded at the same location with a GDD-balanced system and the corrected image of Fig. 6.

In conclusion, we have shown improved phase stability in an OCT system by introduction of an electro-optical phase modulator for carrier generation. We showed that, by digital modification of the source spectrum, sidelobes that are due to spectral modulation could be suppressed. Phase-sensitive digital signal processing for image enhancement has been used for speckle reduction by Yung *et al.*[9] To our knowledge, we have demonstrated for the first time phase-sensitive processing to eliminate GDD in a human skin graft image. Because higher-order dispersion compensation is becoming increasingly important as the OCT source bandwidth increases, postprocessing dispersion compensation could become an attractive alternative to careful dispersion balancing in sample and reference arms. For extremely large bandwidth sources[2] or highly dispersive samples, digital processing also permits dynamic dispersion compensation as a function of depth.

Research grants from the Whitaker Foundation (26083, JFdB), the National Eye Institute (1 R24 EY 12877-01), the U.S. Office of Naval Research (N00014-94-1-0874), the U.S. Department of Energy, and the Beckman Laser Institute Endowment are gratefully acknowledged.

References

1. D. Huang, E. A. Swanson, C. P. Lin, J. S. Schuman, W. G. Stinson, W. Chang, M. R. Hee, T. Flotte, K. Gregory, C. A. Puliafito, and J. G. Fujimoto, "Optical coherence tomography," Science **254,** 1178–1181 (1991).
2. W. Drexler, U. Morgner, F. X. Kartner, C. Pitris, S. A. Boppart, X. D. Li, E. P. Ippen, and J. G. Fujimoto, "*In vivo* ultrahigh-resolution optical coherence tomography," Opt. Lett. **24,** 1221–1223 (1999).
3. G. J. Tearney, B. E. Bouma, and J. G. Fujimoto, "High-speed phase- and group-delay scanning with a grating-based phase control delay line," Opt. Lett. **22,** 1811–1813 (1997).
4. A. M. Rollins, M. D. Kulkarni, S. Yazdanfar, R. Ung-arunyawee, and J. A. Izatt, "*In vivo* video rate optical coherence tomography," Opt. Express **3,** 219–229 (1998), http://www.opticsexpress.org.
5. C. E. Saxer, J. F. de Boer, B. H. Park, Y. Zhao, Z. Chen, and J. S. Nelson, "High-speed fiber-based polarization-sensitive optical coherence tomography of *in vivo* human skin," Opt. Lett. **25,** 1355–1357 (2000).
6. O. E. Martinez, "3000 times grating compressor with positive group velocity dispersion: application to fiber compensation in 1.3–1.6 μm region," IEEE J. Quantum Electron. **23,** 59–64 (1987).
7. M. D. Kulkarni, C. W. Thomas, and J. A. Izatt, "Image enhancement in optical coherence tomography using deconvolution," Electron. Lett. **33,** 1365–1367 (1997).
8. M. Bashkansky, M. D. Duncan, J. Reintjes, and P. R. Battle, "Signal processing for improving field cross-correlation function in optical coherence tomography," Appl. Opt. **37,** 8137–8138 (1998).
9. K. M. Yung, S. L. Lee, and J. M. Schmitt, "Phase-domain processing of optical coherence tomography images," J. Biomed. Opt. **4,** 125–136 (1999).